ADVANCED SCIENCE Open Access
www.advancedscience.com

Artificial Room-Temperature Ferromagnetism of Bulk van der Waals VSe_2

*Jinhyoung Lee, Gunhyoung Kim, Hyunho Seok, Hyunbin Choi, Hyeonjeong Lee, Seokchan Lee, Geonwook Kim, Hyunho Kim, Seowoo Son, Sihoon Son, Dongho Lee, Hosin Hwang, Hyelim Shin, Sujeong Han, Geumji Back, Alexina Ollier, Yeon-Ji Kim, Lei Fang, Gyuho Han, Goo-Eun Jung, Youngi Lee, Hyeong-U Kim, Kenji Watanabe, Takashi Taniguchi, Wonjun Shin, Suraj Cheema, Andreas Heinrich, Won-Jun Jang, and Taesung Kim**

Originating from spin and orbital motion, van der Waals (vdW) ferromagnetism has emerged as a significant platform to experimentally access the fundamental physics of magnetism in reduced dimensions, including quantum computing, sensing, and data storage. However, currently, available vdW ferromagnetic materials can be achieved with mechanical exfoliation and low-temperature operation, which completely limits the monolithic integration of vdW ferromagnets with other functional materials. Nonetheless, the direct synthesis of room-temperature vdW ferromagnets has not been achieved commercially, owing to the imprecise control of the layer-by-layer growth, high-temperature synthesis, and low yield. To overcome these limitations, herein, an artificial vdW ferromagnetic platform has been reported, which activates the nano-crystallization and its corresponding ferromagnetism in bulk VSe_2 via Ar + H_2S plasma sulfurization. Sweeping the magnetic field, vdW ferromagnetism has been spatially resolved, which experimentally correlates with magnetization reversal behavior and domain pinning effects. Furthermore, nano-crystallization of VSe_2 is clearly validated with transmission electron microscopy, energy-dispersive X-ray spectroscopy, X-ray photoelectron spectroscopy, and selected area diffraction analysis. In conclusion, it is envisioned that the artificial vdW ferromagnetic platform can artificially inject the ferromagnetism in bulk vdW VSe_2, which has not been possible previously.

1. Introduction

For centuries, the enigmatic properties of lodestones and their magnetic attraction to iron, as well as the remarkable navigational abilities of birds, fish, and insects across vast distances, have captivated human curiosity. Prior to the advent of electromagnetism and quantum mechanics, it was inconceivable that these phenomena might share a common magnetic foundation.[1] Magnetism, which is as pervasive as the electron itself, fundamentally originated from the motion and spin of elementary particles. Its applications span living organisms, energy harvesting, data storage, and medical diagnostics. When the microscopic "electron magnets" align spontaneously, magnetic order emerges as a fundamental phase of matter, enabling the development of functional devices such as electric generators, motors, magneto-resistive memories, and optical isolators. The electron, often regarded as a minute magnet with two opposing poles, generates a magnetic field through its spin and orbital motion.

J. Lee, H. Lee, G. Kim, D. Lee, T. Kim
School of Mechanical Engineering
Sungkyunkwan University (SKKU)
Suwon-si, Gyeonggi-do 16419, South Korea
E-mail: tkim@skku.edu

The ORCID identification number(s) for the author(s) of this article can be found under https://doi.org/10.1002/advs.202504746

DOI: 10.1002/advs.202504746

J. Lee, A. Ollier, Y.-J. Kim, L. Fang, A. Heinrich, W.-J. Jang
Center for Quantum Nanoscience
Institute for Basic Science (IBS)
Seoul 03760, South Korea

G. Kim, H. Choi, H. Kim, H. Hwang, H. Shin, S. Han, G. Back, W. Shin, T. Kim
Department of Semiconductor Convergence Engineering
Sungkyunkwan University
Suwon 16419, South Korea

H. Seok, S. Lee, S. Son, S. Son, T. Kim
SKKU Advanced Institute of Nanotechnology (SAINT)
Sungkyunkwan University
Suwon 16419, South Korea

H. Seok, S. Lee, S. Son, S. Son, T. Kim
Department of Nano Science and Technology
Sungkyunkwan University
Suwon 16419, South Korea

The collective alignment of these microscopic magnets, driven by intrinsic coupling, raises the emergence of ferromagnetism.[2] However, the Mermin-Wagner theorem[3] suggested that ferromagnetism cannot be persisted in two-dimensional (2D) van der Waals (vdW) systems owing to its thermal fluctuations.

Recent breakthroughs in vdW magnetic crystals have demonstrated that magnetic anisotropy can stabilize long-range magnetic order by creating an excitation gap that counteracts thermal agitation.[4] vdW magnetic crystals serve as ideal platforms for exploring magnetism in reduced dimensions,[5] offering advantages over traditional magnetic thin films. These materials are largely decoupled from substrates,[6] electrically tunable,[7] mechanically flexible,[8] and amenable to chemical functionalization.[9] In early 2017, the first evidence of long-range magnetic order in pristine vdW crystals was reported in $Cr_2Ge_2Te_6$ [10] and CrI_3,[11] both magnetic insulators with distinct properties. Conversely, vdW Fe_3GeTe_2 [12] was identified as a magnetic conductor, highlighting the diverse applications of itinerant magnets [13] and magnetic insulators.[14] Advances in manipulating individual vdW layers have enabled the fabrication of multilayer "designer magnets" [15] with notable outcomes such as giant cross-layer tunneling magnetoresistance [16] through engineered interlayer magnetic coupling. In heterostructures combining electronic and photonic materials, the integration of distinct physical properties can lead to versatile functionalities, including heterostructure multiferroicity,[17] unconventional superconductivity,[18] and the quantum anomalous Hall effect.[19] Major limitations of vdW ferromagnetic heterostructure correspond to the precise kinetic control of stacking order [20] and large-scale control over layer thickness [21] and crystallinity.[22]

To address these challenges, researchers have focused on the extrinsic methods to artificially induce magnetism in non-ferromagnetic vdW crystals. These approaches include i) defect engineering through vacancies, adatoms, grain boundaries, or edges; [23] ii) substitution of magnetic species; [24] and iii) the magnetic proximity effect,[25] where vdW materials are interfaced with magnetic substrates. However, establishing long-range correlations between extrinsically introduced magnetic moments remains difficult, and substrate-induced magnetic responses are often limited. Theoretical proposals for inducing ferromagnetism by modifying lattice and band structures have yet to be experimentally realized, arising from the intrinsic vdW lattice structure. In contrast, when ferromagnetism originating from its vdW lattice structure can be experimentally realized, it will drive the versatile advances for vdW ferromagnets [2] and their corresponding applications for electronic,[26] spintronics,[27] and next-generation quantum devices.[28] These underlying limitations of the conventional vdW ferromagnets motivated us to develop an on-demand synthesis method of vdW ferromagnet.

Herein, we report an artificial vdW ferromagnetic platform for non-magnetic vdW crystals, which provides a systematic solution for conventional vdW ferromagnets. To artificially activate the ferromagnetism in bulk vdW VSe_2, lattice distortion has been conducted with Ar + H_2S plasma sulfurization, which corresponds to the ion penning effects and ion penetration. The artificial vdW ferroelectricity activates the ferromagnetic manipulation regardless of the number of vdW layers, which comprehensively overcomes the limitations of conventional vdW ferromagnetism. Artificial vdW ferromagnetism was locally observed with Magnetic Force Microscopy (MFM) imaging. The MFM junction was constructed using a Co-coated magnetic tip, magnetically shielded sample holder, and dual-permanent-magnet generator capable of sweeping the in-plane magnetic field from -500 to +500 Oe. The spatial resolution of magnetic domains was achieved by decoupling topography and magnetic force measurements at controlled tip-sample distances (5 and 25 nm, respectively). [[According to the direction of the magnetic field of the MFM junction, vdW ferromagnetism has been spatially resolved with local ferromagnetic domain mapping of nano-crystallized VSe_2, which experimentally correlates with magnetization reversal behavior and domain pinning effects. Furthermore, nano-crystallization of VSe_2 was clearly validated with atomic force microscopy (AFM), transmission electron microscopy (TEM), energy-dispersive X-ray spectroscopy (EDS), X-ray photoelectron spectroscopy (XPS), selected area diffraction (SAED) and Raman spectra measurements. In conclusion, we envision that our artificial vdW ferromagnetic platform can artificially manipulate the ferromagnetism in bulk vdW VSe_2 via nano-crystallization, which has not been possible previously. Unlike previously reported intrinsic room-temperature vdW ferromagnets such as $Cr_{1+x}Te_2$,[31] Fe_5GeTe_2 [32] and Fe_3GaTe_2,[33] which rely on defined magnetic ordering. Nevertheless, critical challenges persist, including intricate magnetic interactions across atomic lattices, scalability limi-

G. Han, G.-E. Jung, Y. Lee
Park Systems Corporation
109, Gwanggyo-ro, Yeongtong-gu, Suwon-si, Gyeonggi-do 16229, South Korea

H.-U Kim
Semiconductor Manufacturing Research Center
Korea Institute of Machinery and Materials (KIMM)
Daejeon 34103, South Korea

H.-U Kim
Nano-Mechatronics
KIMM Campus
University of Science & Technology (UST)
Daejeon 34113, South Korea

K. Watanabe, T. Taniguchi
National Institute for Materials Science
Namiki 1-1
Tsukuba, Ibaraki 305-0044, Japan

H. Seok, S. Cheema
Research Laboratory of Electronics
Massachusetts Institute of Technology
Cambridge, MA 02139, USA

S. Cheema
Department of Electrical Engineering and Computer Science
Massachusetts Institute of Technology
Cambridge, MA 02139, USA

H. Seok, S. Cheema
Department of Materials Science and Engineering
Massachusetts Institute of Technology
Cambridge, MA 02139, USA

A. Ollier, A. Heinrich, W.-J. Jang
Department of Physics
Ewha Womans University
Seoul 03760, South Korea

T. Kim
Department of Nano Engineering
Sungkyunkwan University
Suwon 16419, South Korea

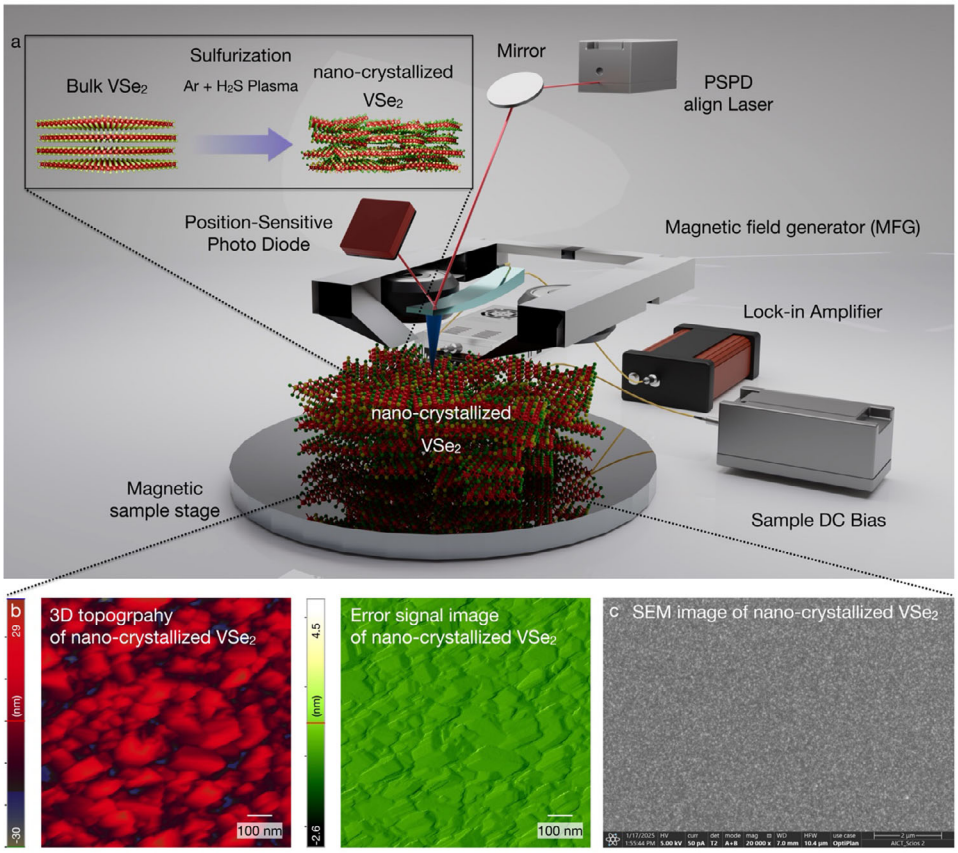

Figure 1. Artificial vdW ferromagnetic platform for bulk VSe_2. a) Schematic illustration of the artificial vdW ferromagnetic platform, which has been achieved with (i) Ar + H_2S plasma and (ii) MFM junction. To spatially resolve the ferromagnetism, an MFM junction has been constructed with a magnetic field generator, magnetic sample holder, and Co-coated magnetic tip, which excludes the generation of the electrical field at the tip-sample junction. b) AFM image (left side as 3D topography image, right side as error signal image) and c) SEM image of nano-crystallized VSe_2.

tations in synthetic methodologies, and inherent interfacial inhomogeneity. Our approach enables artificial vdW ferromagnetism via nano-crystallization in vdW VSe_2. We envision that this strategy provides the artificial injection of the vdW ferromagnetism, offering the versatile advances in 2D vdW spintronic systems.

2. Results and Discussion

2.1. Artificial vdW Ferromagnetic Platform for Bulk VSe_2

To artificially induce the ferromagnetism of the bulk vdW 1T-VSe_2 (non-magnetic), single-step penetrative plasma sulfurization has been utilized to inject the ferromagnetism in bulk vdW VSe_2 via hydrogen sulfide (H_2S) + argon (Ar) ion bombardment, which results in the lattice distortion and nano-crystallization.[34] In our previous research, H_2S + Ar ion bombardment generates the nano-crystallization in van der Waals materials, offering a synthetic platform to isolate the VSe_2 monolayer for versatile magnetic functionalities. In this study, this approach has been extended to distort the vdW lattice in non-magnetic bulk VSe_2, enabling the emergence of ferromagnetism through the VSe_2 monolayer isolation. The monolayer VSe_2 (1T and 2H phase) is notable for its intrinsic ferromagnetism owing to the strong electron coupling in the $3d^1$ odd-electronic configuration of V^{4+}.[30] Astonishingly, the ferromagnetic ordering of monolayer VSe_2 is robust and persists above room temperature, making monolayer VSe_2 a significant material for vdW spintronics applications.[35] However, the monolayer VSe_2 is vulnerable to oxidation,[21] which vanishes the ferromagnetism of monolayer VSe_2. Unlike the monolayer VSe_2, bulk vdW VSe_2 indicates non-magnetic properties. Thus, bulk vdW VSe_2 was intentionally selected for artificial ferromagnetism injection with nano-crystallization. As shown in **Figure 1a**, the nano-crystallized VSe_2 was fabricated in the following three steps. First, bulk vdW VSe_2 was mechanically exfoliated and transferred onto a SiO_2/Si wafer. Second, single-step penetrative plasma sulfurization (RF power 400 W) was conducted to crystallize the bulk vdW VSe_2. Third, the MFM junction was constructed for nanoscale observation of the magnetic domain distribution, constructed with a Co-coated magnetic tip (Figure S1, Supporting Information), magnetic sample holder, and magnetic field generator (Figures S2 and S3, Supporting Information), enabling the spatial observation of ferromagnetic characteristics. Also, nano-crystallization of VSe_2 has been observed with AFM and SEM imaging. As shown in Figure 1b, nano-crystallization of VSe_2 has been experimentally revealed within the AFM 3D topography image and error signal image. Furthermore, an SEM image of nano-crystallized VSe_2 correlatively indicates the nanoscale crystallization. The grain

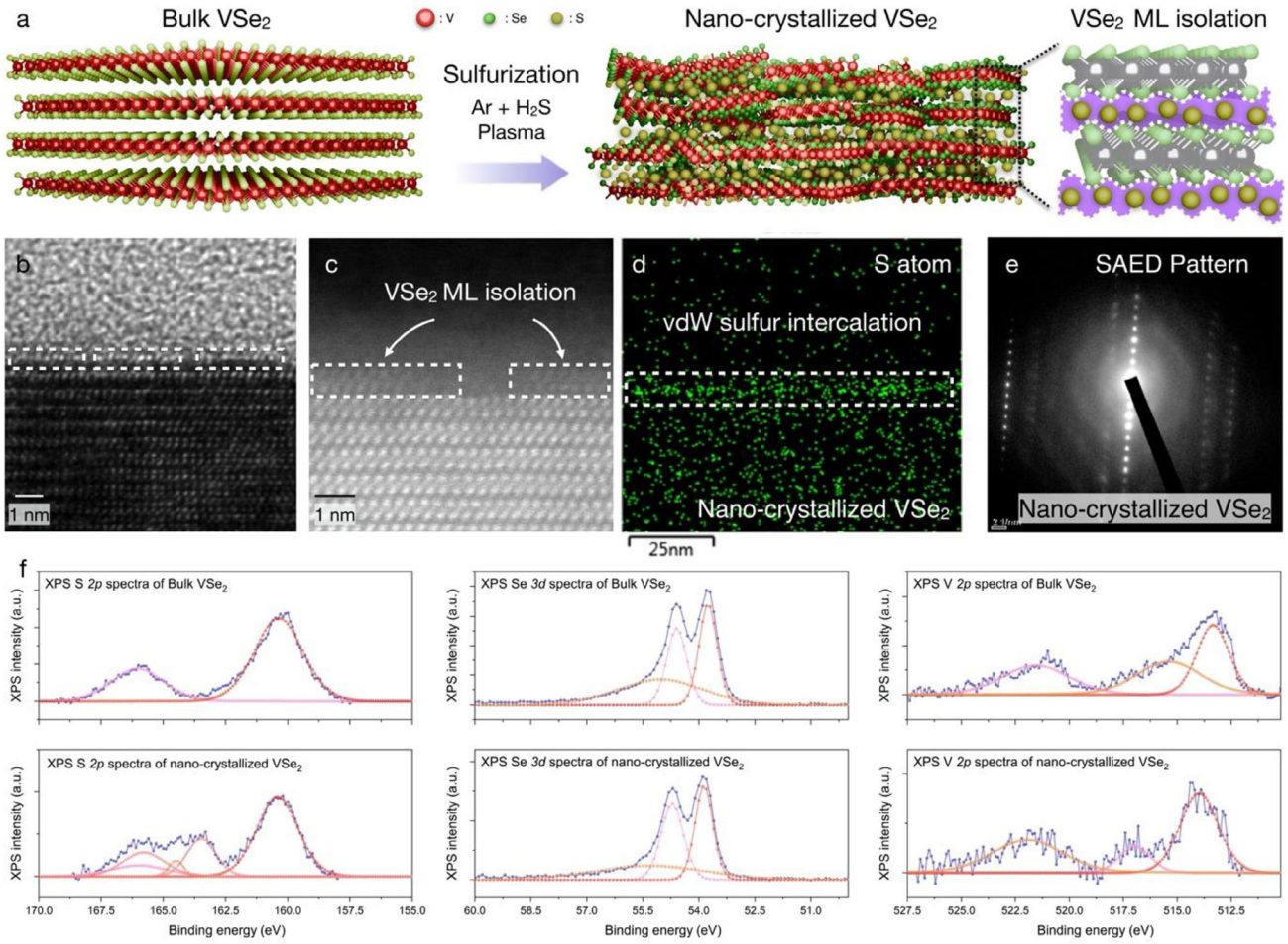

Figure 2. Cross-sectional observation of nano-crystallized VSe_2 via Ar + H_2S plasma. a) Schematic illustration of nano-crystallized VSe_2, generating the VSe_2 ML isolation. b) Cross-sectional analysis of nano-crystallized VSe_2 with HR-TEM and STEM image. Cross-sectional d) EDS mapping and e) SAED patterns of nano-crystallized VSe_2, which is configured with RF plasma 400 W. f) XPS spectra of V *2p*, Se *3d*, S *2p*, exhibiting the sulfurization of bulk vdW VSe_2 with emergence of V-S bonding in S *2p* spectra.

size of nano-crystallized VSe_2 is distributed as a function of RF plasma power (18.2–45.7 nm).[36] MFM domain imaging reveals that the magnetic domain size corresponds with the nanograin size, resulting in grain boundaries operating as pinning sites. For the improvement of large-scale uniformity, inductively coupled plasma (ICP) systems have been utilized to ensure homogeneous ion bombardment over centimeter-scale substrates.

2.2. Cross-Sectional Observation of Nano-Crystallized VSe_2

Furthermore, cross-sectional TEM images of nano-crystallized VSe_2 were experimentally obtained, exhibiting the VSe_2 monolayer isolation and its corresponding lattice distortion, as shown in **Figure** 2a–c. The emergence of room-temperature ferromagnetism in bulk VSe_2 is attributed to the VSe_2 monolayer isolation via nano-crystallization. The nano-crystallization process, driven by local lattice strain during the plasma sulfurization, disrupts interlayer coherence and effectively decouples adjacent VSe_2 layers. This structural decoupling yields electronically quasi-2D regions where ferromagnetism prevails, thereby facilitating ferromagnetic ordering via Stoner-type instability. Concurrently, the localized symmetry breaking enhances orbital contributions to magnetism, further enhancing and stabilizing the ferromagnetic behavior. Collectively, these effects enable the realization of robust ferromagnetism at room temperature in an otherwise nonmagnetic bulk VSe_2 system. Cross-sectional EDS mapping and SAED pattern were correlated to nano-crystallization. As Bulk vdW VSe_2 corresponds to Figure S4 (Supporting Information), Figure 2d indicates the nano-crystallized VSe_2, comparing the effects of nano-crystallization. While the EDS mapping indicates the intrinsic distribution of the V atom, Se atom, C atom, and S atom in bulk states, the distribution of the S atom has been dominantly generated at the surface after the nano-crystallization. As plasma sulfurization is configured with Ar + H_2S plasma, resulting in the amorphous phase of Bulk vdW VSe_2 and nano-crystallization. The SAED pattern of 1T- VSe_2 indicates the periodic pattern, while the nano-crystallized VSe_2 lattice (Figure 2e) experimentally clarifies the origin of the observed unidirectional lattice,[37] which corresponds to the lattice distortion. XPS mea-

surements were performed to clarify and elucidate variations of chemical bonding within nano-crystallization, as shown in Figure 2f. As the V *2p* XPS spectra of pristine VSe_2 have been deconvoluted into the binding energy of 513.3 eV peak, 521.6, and 515.4 eV, each peak has been shifted as 517.0, 514.0, 521.9 eV with nano-crystallization and its corresponding V-S bonding formation. Also, S *2p* XPS spectra of pristine VSe_2 can be separated as 166.0 eV peak and 160.4 eV peak. After crystallization, an additional deconvoluted S *2p* peak has been generated as 164.5, 163.5, and 165.8 eV. Thus, V—S bonding formation and nano-crystallization can be further clarified with a comparison of S *2p* spectra. Se *3d* peak also exhibits heterogeneity in chemical composition, which can be deconvoluted as 54.6, 53.8, and 55 eV peaks. And Se *3d* peak has been shifted to 54.7, 53.9, and 55.3 eV, which directly corresponds to the Se atom termination with sulfurization. Owing to the ion penning effects, Se atoms were locally terminated by S atoms via plasma sulfurization, which resulted in a substantial increase in the S/Se atomic concentration ratio. The Se-to-S substitution ratio was quantified from XPS atomic concentration analysis, yielding sulfur incorporation of ≈11.45 at%, while selenium incorporation exhibits ≈7.30 at% at the nano-crystallized VSe_2 (400 W). In our sulfurization system, the sufficient generation of H_2S^+ for bombardment on VSe_2 to crystallize the lattice is most significant. The proposed mechanism of H_2S^+ generation in this system is the Penning effect by the Ar gas and the direct ionization of H_2S as follows Equations (1) and (2).[38]

$$Ar + e^- \rightarrow Ar^+ + 2e^- \quad (1)$$

$$Ar^+ + H_2S \rightarrow Ar + H_2S^+ \quad (2)$$

Sufficient electrons in the plasma system can directly ionize H_2S gas to generate H_2S^+, as shown in Equation (3). But except for Ar gas, it is difficult to generate H_2S plasma owing to the low ionization energy characteristics of H_2S gas.[39] To prevent plasma-induced over-etching and maintain the integrity of the layered VSe_2 structure, plasma conditions were carefully optimized. The gas mixture was fixed at a 1:1 ratio of Ar and H_2S (50 sccm each), and RF plasma power was set at 400 W. These conditions were found to be optimal for inducing nano-crystallization without significant damage to the surface or delamination. Preliminary experiments with higher RF power (>500 W) or an Ar-rich environment resulted in structural degradation and amorphization.

$$e^- + H_2S^+ \rightarrow 2e^- \quad (3)$$

For the precise control of plasma-based sulfurization, the gas mixture ratio was fixed as Ar and H_2S as 1:1 (50 sccm injection for each gas). In the bulk plasma, multi-chain reactions (Equations 1–3) lead to an increase in plasma potential, while the substrate remains grounded. This creates a self-biased system that induces an electric field (sheath region), accelerating positively charged ions (H_2S^+ and Ar^+) toward the substrate and resulting in ion bombardment. This simultaneous ion bombardment on the single-crystal VSe_2 surface induces lattice distortion, breaking the long-range crystallinity and transforming the surface into a nanoscale, discontinuous crystalline structure. With continued ion exposure, the bombardment penetrates deeper, affecting several vdW layers beneath the surface. Consequently, a few upper layers become nanocrystalline and structurally disordered, while the underlying bulk retains its pristine single-crystalline structure. This VSe_2 monolayer isolation exhibits emergent ferromagnetic behavior, in contrast to the non-ferromagnetic nature of pristine single-crystalline VSe_2. The concurrent Ar^+ and H_2S^+ ion bombardment onto single-crystalline VSe_2 leads to a high density of nanoscale defects, which disrupts the long-range order and results in nanoscale discontinuous domains of VSe_2. This ion-induced lattice distortion promotes the formation of nanocrystalline structures (Figure S5, Supporting Information). Similar nano-crystallization phenomena have been observed in various systems, including wafer-scale MoS_2–WS_2 vertical heterostructures,[40] WS_2–graphene interfaces,[6] and other TMDC-based heterostructures through plasma-enhanced chemical vapor deposition (PECVD).

2.3. Spatially-Resolved Ferromagnetic Behavior of Nano-Crystallized VSe_2

To observe the artificially generated ferromagnetic domain, MFM image has been correlatively conducted with i) magnetic imaging and ii) topography imaging, which allows the observation of long-range magnetic interactions while minimizing the influence of the topography. While the topography imaging was conducted within a tip-sample distance of ≈5 nm, which affects the vdW interaction, magnetic force can be clearly obtained with a tip-sample distance of ≈25 nm. For magnetic field sweep, a magnetic field generator has been attached to control the magnetic field at the MFM junction. A magnetic field generator was constructed with two permanent magnets. With a fixed permanent magnet, the rotation of another permanent magnet locally induces an in-plane magnetic field at the tip apex between the soft iron localizers. Rotating the permanent magnet results in a controllable magnetic field between the minimum magnetic field (−500 Oe) and the maximum magnetic field (+500 Oe). The magnetic field can be controlled at the tip-sample junction, the magnetic hysteresis can be spatially resolved, as shown in **Figure 3a**. As the magnetic field was controlled within 250 Oe duration, the yellow dash box MFM phase images sequentially resolved as -147.46° (-500 Oe), -148.21° (-250 Oe), -147.43° (0 Oe), 37.95° (+250 Oe), 39.10° (+500 Oe), 38.96° (+500 Oe), 37.01° (+250 Oe), 34.88° (0 Oe), -146.90° (-250 Oe), -149.0° (-500 Oe). In contrast, the white dashed box in the MFM phase image can be mapped as 38.90° (-500 Oe), -39.28° (-250 Oe), -37.16° (0 Oe), -144.63° (+250 Oe), -146.72° (+500 Oe), -145.18° (+500 Oe), -145.94° (+250 Oe), -145.16° (0 Oe), 38.55° (-250 Oe), 39.04° (-500 Oe). Furthermore, the ferromagnetic hysteresis curve has been mapped from spatially extracted ferromagnetic phase value from each dashed box, as shown in Figure 3b. Owing to the MFM phase mapping, the nanoscale ferromagnetic domain has been experimentally observed with room-temperature ferromagnetic hysteresis behavior. Regarding the emergence of room-temperature ferromagnetism in bulk VSe_2 upon Ar + H_2S plasma treatment, the synergistic mechanism has been attributed to i) orbital magnetism and ii) vdW sulfur intercalation, which effectively isolates monolayer VSe_2 regions at the bulk VSe_2 crystal. First, the

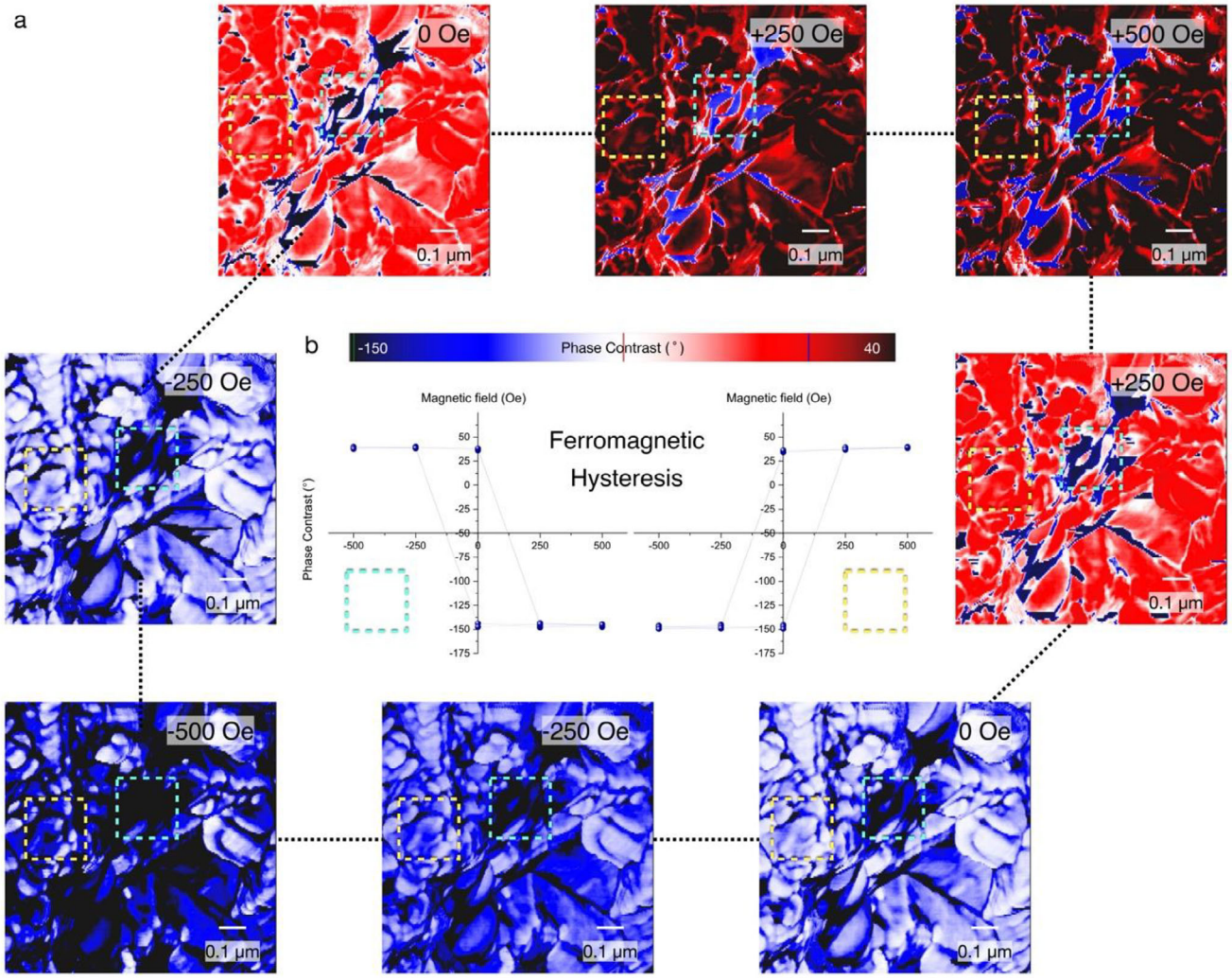

Figure 3. Spatially-resolved ferromagnetism of nano-crystallized VSe_2. Resolving the nanoscale magnetic heterogeneity and ferromagnetic hysteresis behavior via magnetic domain imaging. a) sequential MFM phase images of nano-crystallized VSe_2, which has been generated by the magnetic field control. b) Ferromagnetic hysteresis mapping with nanoscale magnetic domain extraction from the selected yellow box (left) and white box (right).

nano-crystallization process introduces substantial local strain and atomic disorder into the VSe_2 lattice. These structural perturbations break the spatial inversion symmetry and promote the localization of vanadium 3d orbitals, thereby enhancing orbital magnetic moments. Such orbital contributions are known to play a critical role in transition metal dichalcogenide systems under reduced symmetry, enabling finite magnetization even in the absence of conventional spin ordering. Density functional theory (DFT) calculations on disordered VSe_2 supercells further support this scenario, indicating non-zero net magnetic moments arising from asymmetric d-orbital occupancy.[41] Second, the incorporation of sulfur atoms during H_2S plasma exposure induces the intercalation of sulfur species into the vdW gaps between VSe_2 layers. This interlayer sulfur intercalation disrupts the electronic coherence along the c-axis, effectively decoupling adjacent VSe_2 layers and inducing quasi-monolayer behavior within localized crystalline domains. Previous theoretical and experimental studies have established that monolayer VSe_2 favors itinerant ferromagnetism due to Stoner-type instability at the Fermi level,[42] a behavior suppressed in the bulk form due to strong interlayer hybridization. Our results suggest that the plasma-induced sulfur intercalation restores the monolayer-like electronic structure within nano-crystallized grains, enabling ferromagnetic ordering at room temperature. Thus, the emergence of room-temperature ferromagnetism in sulfurized VSe_2 arises from a cooperative interplay between orbital magnetism driven by lattice disorder and monolayer isolation effects. This post-synthetic mechanism represents a novel pathway to modulate the ferromagnetic order in otherwise non-magnetic vdW materials.

2.4. Nano-Crystallization Effects in the Artificially Generated Ferromagnetic Domain

Within the magnetic field weep, MFM phase (**Figure** 4a) and MFM amplitude (Figure 4b) from opposite magnetic fields

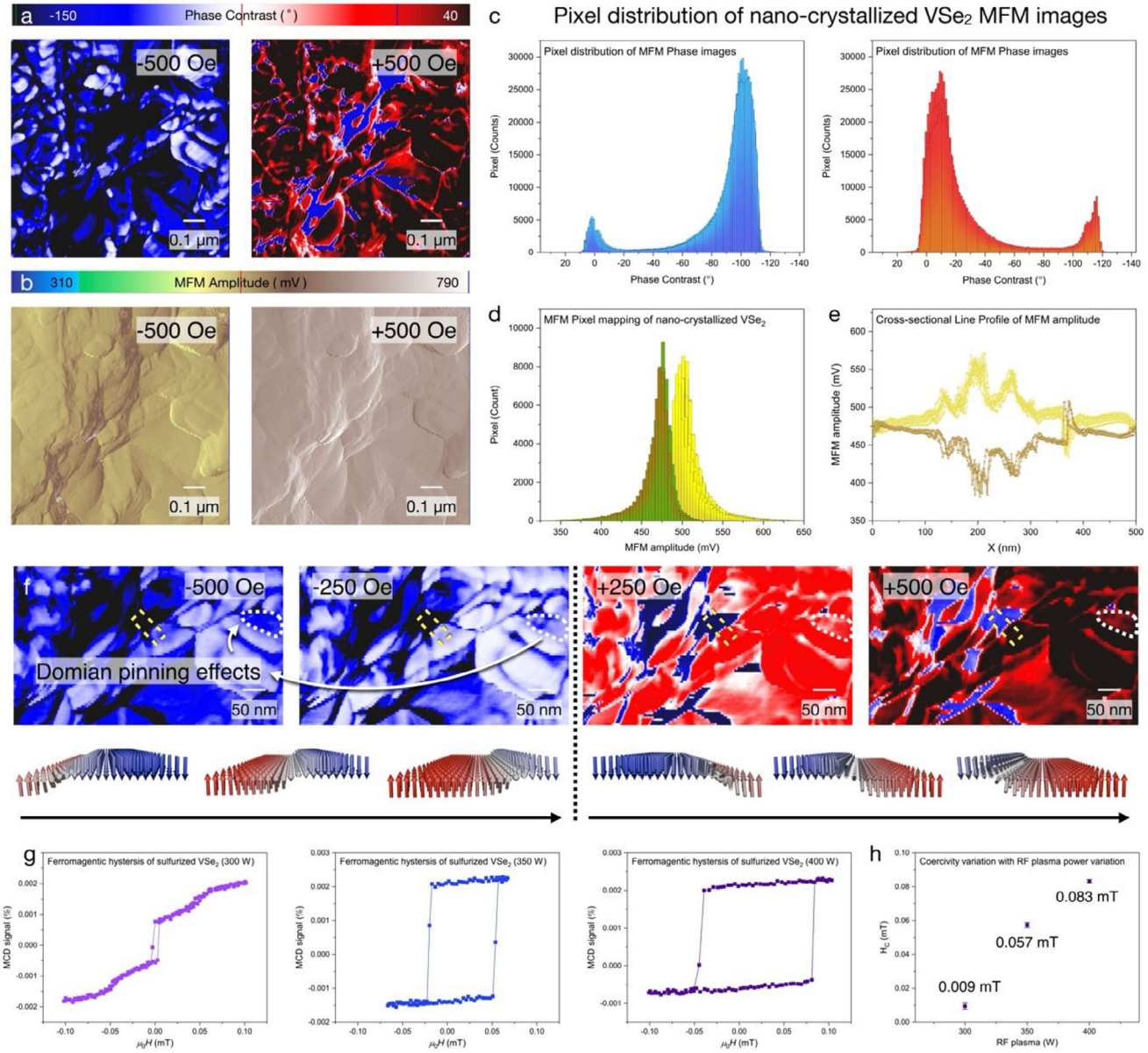

Figure 4. Reversible magnetization of nano-crystalline ferromagnetic domain. a) MFM phase images (top) and b) MFM amplitude images (bottom) with a heterogeneous magnetic field. Pixel distribution of nano-crystallized VSe_2, consisted of c) MFM phase and d) MFM amplitude. e) Cross-sectional line profiles of MFM amplitude, which indicates magnetization reversal of nano-crystallized VSe_2. f) Sequential domain dynamics with magnetic field sweep, resulting in the magnetization reversal of the ferromagnetic domain. g) ferromagnetic hysteresis with RF plasma power variation and its corresponding h) coercivity.

(+500 Oe, -500 Oe) correspond to the magnetization reversal, which fully operates as a reversible magnet. Furthermore, statistical analysis with nano-crystallized VSe_2 MFM pixel distribution has been conducted, as shown in Figure 4c,d.

As shown in Figure 4c, the dominant pixel peak from +500 Oe corresponds to the MFM phase as -101.89°, while the dominant pixel peak with −500 Oe has been extracted as 1.36°. Additionally, MFM amplitude pixel mapping exhibits heterogeneous peak distribution of 505.67° and 476.45°, correlating the existence of the heterogeneous magnetic pole (Figure 4d). Such reversible pixel distribution from MFM phase and MFM amplitude images directly supports the magnetization reversal. The cross-sectional line profile of nano-crystallized VSe_2 corresponds to the magnetization reversal within magnetic field control (Figure 4e). To verify that the nano-crystallization effects for ferromagnetism, magnetization reversal (Figure S6, Supporting Information), and domain pinning effects were also resolved with MFM amplitude images (Figure 4f). Within the maximum magnetic field (+500 Oe, -500 Oe), domain distribution of +250 Oe, -250 Oe has been expanded owing to the atomic-scale defects from nano-crystallization, which induces the domain pinning effects. The emergence of the nanoscale ferromagnetic domain can be ex-

plained with nano-crystallization. When pinning effects are negligible, magnetic domain walls can be spatially shifted and expanded without significant domain wall resistance, leading to high initial magnetization within a minimum external magnetic field. However, the existence of defects enhances the energy barrier of ferromagnetic domain wall movements, which completely blocks the spatial domain wall movements. Regarding the high defect density of nano-crystallized VSe_2, the magnetization rises gradually until the external magnetic field is as large as the pinning energy. To further validate the room-temperature ferromagnetism of nano-crystallized VSe_2, bulk VSe_2 has been investigated with MFM imaging and its corresponding pixel distribution mapping (Figures S7–S10, Supporting Information). As bulk VSe_2 exhibits non-magnetic properties, magnetization reversal, ferromagnetic hysteresis, and domain pinning effects were not experimentally observed, unlike nano-crystallized VSe2. To verify the room-temperature ferromagnetism observed via MFM, superconducting quantum interference device (SQUID) magnetometry was performed on nano-crystallized VSe_2. As shown in Figure 4g, the M–H loop at 300 K demonstrates the enlargement of ferromagnetic hysteresis and its corresponding coercivity as ≈0.009 mT (300 W), 0.057 mT (350 W), and 0.083 mT (400 W). Plasma-dependent coercivity further indicates a nano-crystallization of bulk VSe2, substantiating the room-temperature ferromagnetic behavior in our system.

3. Conclusion

In conclusion, an artificial room-temperature vdW ferromagnetism has been achieved in VSe_2 through nano-crystallization with plasma sulfurization. Owing to the ion bombardment, the Se atom is randomly terminated to the S atom, resulting in the VSe_2 monolayer isolation and local lattice distortion. By constructing the MFM junction with nano-crystallized VSe2, vdW ferromagnetism, and its corresponding ferromagnetic hysteresis curve have been spatially resolved. Nano-crystallization of bulk vdW VSe_2 was also correlatively observed with cross-sectional transmission electron microscopy, energy-dispersive X-ray spectroscopy, and selected area diffraction analysis. In conclusion, our artificial room-temperature vdW ferromagnetic platform can offer an extendable platform for vdW ferromagnetic material, which enables the vdW ferromagnets to be accessible, engineerable, and integrable into emergent heterostructures for previously unachieved.

4. Experimental Section

Nano-Crystallization: The ICP-type of plasma-enhanced chemical vapor deposition (ICP-PECVD) (AFS-IC6T, Korea) was used for the crystallization of VSe_2 to induce its amorphous phase. A high vacuum of $\approx 5 \times 10^{-5}$ in the PECVD chamber was used to evacuate impurities to achieve clean synthesis without other unexpected reactions before plasma treatment for nano-crystallization. In this study, only the RF plasma power was fixed as 400 W under constant gas conditions, and the argon and H_2S flows were maintained at 50 SCCM at a pressure of 25 mTorr at room temperature.

Mechanical Exfoliation and Transfer of vdW VSe_2: Before mechanical exfoliation and dry transfer, a polydimethylsiloxane stamp was attached to a glass cover. vdW VSe_2 was mechanically exfoliated from bulk crystals (HQ Graphene, Netherlands) onto polydimethylsiloxane stamps and then transferred onto the substrate by applying a transfer condition of 70 °C.

Magnetic Force Microscopy: MFM (NX-10 AFM, Park Systems, Republic of Korea) was conducted with an MFMR cantilever. The MFMR cantilever was calibrated with a tip radius of 25 nm, a length of 225 µm, a height of 15 µm, a width of 28 µm, and a spring constant of 2.8 N/m, resulting in a resonance frequency of 75 kHz. A magnetic sample holder was loaded to block the electrical field generation at the MFM junction. Additionally, a magnetic field generator was further attached to artificially induce the magnetic field and observe the magnetic hysteresis, which was spatially resolved at the MFM junction. Before the MFM measurements, the MFM tip was magnetized as an "N" pole for 15 min.

Material Characterization: XPS measurements (XIS Supra+, Kratos, United Kingdom) were used to characterize VSe_2, with an X-ray spot size of 400 µm. Peak deconvolution was performed on the V 2*p*, Se 2*p*, and S 2*p* signals, with the profiles aligned using the C 1s peak at 285 eV. The XPS data were calibrated using the CASAXPS software (version 8.1). Optical microscopy (U-MSSP4, Olympus, Japan) and FE-SEM (S-4800, Hitachi, Japan) were used to examine the transferred flakes. For cross-sectional TEM specimen preparation, a focused ion beam instrument (NX2000, Hitachi Ltd., Japan) was used, employing a Ga^+ ion beam (30–5 keV) and a lift-off process to etch the specimens. TEM (JEM-2100F, JEOL, Japan) and XRD (Empyrean, Malvern PANalytical, United Kingdom) were used to observe the lattice structure, EDS, and SAED patterns of the layered VSe_2 structures at the atomic scale.

Supporting Information

Supporting Information is available from the Wiley Online Library or from the author.

Acknowledgements

This research was supported by the Basic Science Research Program of the National Research Foundation of Korea (NRF) funded by the Ministry of Education (No. 2022R1A3B1078163). This study was supported by the Institute for Basic Science (grant number IBS-R027-D1). This work was supported by the Korean Collaborative & High-tech Initiative for Prospective Semiconductor Research (K-CHIPS) (20024772), funded by the Ministry of Trade, Industry & Energy (MOTIE, Korea). This study was supported by the MOTIE (Ministry of Trade, Industry, and Energy (grant number 1415187508) for the development of future semiconductor devices. This study was supported by the National Research Foundation (NRF) funded by the Korean government (MSIT) (No. RS-2024-00437142). This work was supported by the Technology Innovation Program (20017367, Development of precise manufacturing technology for CMP pad conditioners), funded By the Ministry of Trade, Industry & Energy (MOTIE, Korea).

Conflict of Interest

The authors declare no conflict of interest.

Author Contributions

J.L., G.K., H.S., H.C. contributed equally to this work. J.L., G.K., H.S., and H.C. prepared samples and performed experiments. H.L., S.L., G.K., H.K., S.S., S.S., and D.L. performed the technical discussions on plasma sulfurization. H.S., S.H., G.B., H.H. conducted the analytical experiments, including TEM, EDS, and XPS measurements. G.H., G.J., and Y.L. provided technical advice on the MFM system and magnetic field generator. T.T. and K.W. provide the bulk hexagonal boron nitride samples. A.O., Y.K., and L.F. A.H., W.J., W. S., S.C., H.K., J.L., G.K., H.S., H.C. and T.K. wrote the manuscript with contributions from all the authors. T.K. designed and supervised the study. All the authors have read and approved the final version of this manuscript.

Data Availability Statement

The data that support the findings of this study are available from the corresponding author upon reasonable request.

Keywords

ferromagnetic, magnetic force microscopy, nano-crystallization, van der Waals materials, vanadium selenide

Received: March 15, 2025
Revised: April 22, 2025
Published online: May 30, 2025

[1] O. Gutfleisch, M. A. Willard, E. Brück, C. H. Chen, S. Sankar, J. P. Liu, *Adv. Mater.* **2011**, *23*, 821.
[2] J. Chu, Y. Wang, X. Wang, K. Hu, G. Rao, C. Gong, C. Wu, H. Hong, X. Wang, K. Liu, *Adv. Mater.* **2021**, *33*, 2004469.
[3] M. V. Fischetti, W. G. Vandenberghe, *Phys. Rev. B* **2016**, *93*, 155413.
[4] D. Makarov, O. M. Volkov, A. Kákay, O. V. Pylypovskyi, B. Budinská, O. V. Dobrovolskiy, *Adv. Mater.* **2022**, *34*, 2101758.
[5] K. S. Burch, D. Mandrus, J.-G. Park, *Nature* **2018**, *563*, 47.
[6] H. Seok, M. Kim, J. Cho, S. Son, Y. T. Megra, J. Lee, M. G. Nam, K. W. Kim, K. Aydin, S. S. Yoo, *Adv. Mater.* **2024**, 2411211.
[7] K. Aydin, M. Kim, H. Seok, C. Bae, J. Lee, M. Kim, J. Park, J. T. Hupp, D. Whang, H. U. Kim, *Energy Environ. Mater.* **2025**, *8*, 12800.
[8] J. Lee, G. Woo, J. Cho, S. Son, H. Shin, H. Seok, M.-J. Kim, E. Kim, Z. Wang, B. Kang, *Nat. Commun.* **2024**, *15*, 5162.
[9] X. Chen, A. R. McDonald, *Adv. Mater.* **2016**, *28*, 5738.
[10] G. Lin, H. Zhuang, X. Luo, B. Liu, F. Chen, J. Yan, Y. Sun, J. Zhou, W. Lu, P. Tong, *Phys. Rev. B* **2017**, *95*, 245212.
[11] S. Jiang, L. Li, Z. Wang, K. F. Mak, J. Shan, *Nat. Nanotechnol.* **2018**, *13*, 549.
[12] B. Chen, J. Yang, H. Wang, M. Imai, H. Ohta, C. Michioka, K. Yoshimura, M. Fang, *J. Phys. Soc. Jpn.* **2013**, *82*, 124711.
[13] H. Li, S. Ruan, Y. J. Zeng, *Adv. Mater.* **2019**, *31*, 1900065.
[14] J. Liu, T. Hesjedal, *Adv. Mater.* **2023**, *35*, 2102427.
[15] D. Zhong, K. L. Seyler, X. Linpeng, R. Cheng, N. Sivadas, B. Huang, E. Schmidgall, T. Taniguchi, K. Watanabe, M. A. McGuire, *Sci. Adv.* **2017**, *3*, 1603113.
[16] W. Zhu, H. Lin, F. Yan, C. Hu, Z. Wang, L. Zhao, Y. Deng, Z. R. Kudrynskyi, T. Zhou, Z. D. Kovalyuk, *Adv. Mater.* **2021**, *33*, 2104658.
[17] T. Han, Z. Lu, G. Scuri, J. Sung, J. Wang, T. Han, K. Watanabe, T. Taniguchi, L. Fu, H. Park, *Nature* **2023**, *623*, 41.
[18] Y. Cao, V. Fatemi, S. Fang, K. Watanabe, T. Taniguchi, E. Kaxiras, P. Jarillo-Herrero, *Nature* **2018**, *556*, 43.
[19] Z. Lu, T. Han, Y. Yao, A. P. Reddy, J. Yang, J. Seo, K. Watanabe, T. Taniguchi, L. Fu, L. Ju, *Nature* **2024**, *626*, 759.
[20] S. Wang, X. Cui, C. e. Jian, H. Cheng, M. Niu, J. Yu, J. Yan, W. Huang, *Adv. Mater.* **2021**, *33*, 2005735.
[21] W. Yu, J. Li, T. S. Herng, Z. Wang, X. Zhao, X. Chi, W. Fu, I. Abdelwahab, J. Zhou, J. Dan, *Adv. Mater.* **2019**, *31*, 1903779.
[22] Z. Zhang, J. Niu, P. Yang, Y. Gong, Q. Ji, J. Shi, Q. Fang, S. Jiang, H. Li, X. Zhou, *Adv. Mater.* **2017**, *29*, 1702359.
[23] R. Nair, I.-L. Tsai, M. Sepioni, O. Lehtinen, J. Keinonen, A. V. Krasheninnikov, A. C. Neto, M. Katsnelson, A. Geim, I. Grigorieva, *Nat. Commun.* **2013**, *4*, 2010.
[24] S. Hébert, C. Martin, A. Maignan, R. Retoux, M. Hervieu, N. Nguyen, B. Raveau, *Phys. Rev. B* **2002**, *65*, 104420.
[25] E. M. Choi, K. I. Sim, K. S. Burch, Y. H. Lee, *Adv. Sci.* **2022**, *9*, 2200186.
[26] J. Lee, G. Woo, G. Lee, J. Jeon, S. Lee, Z. Wang, H. Shin, G.-W. Lee, Y.-J. Kim, D.-H. Lee, *ACS Appl. Mater. Interfaces* **2024**, *16*, 35505.
[27] L. Guo, S. Hu, X. Gu, R. Zhang, K. Wang, W. Yan, X. Sun, *Adv. Mater.* **2024**, *36*, 2301854.
[28] J. Lee, E. Kim, J. Cho, H. Seok, G. Woo, D. Yu, G. Jung, H. Hwangbo, J. Na, I. Im, *Adv. Sci.* **2024**, *11*, 2305512.
[29] P. M. Coelho, K. Nguyen Cong, M. Bonilla, S. Kolekar, M.-H. Phan, J. Avila, M. C. Asensio, I. I. Oleynik, M. Batzill, *J. Phys. Chem. C* **2019**, *123*, 14089.
[30] M. Bonilla, S. Kolekar, Y. Ma, H. C. Diaz, V. Kalappattil, R. Das, T. Eggers, H. R. Gutierrez, M.-H. Phan, M. Batzill, *Nat. Nanotechnol.* **2018**, *13*, 289.
[31] X. Zhang, Q. Lu, W. Liu, W. Niu, J. Sun, J. Cook, M. Vaninger, P. F. Miceli, D. J. Singh, S.-W. Lian, *Nat. Commun.* **2021**, *12*, 2492.
[32] A. F. May, D. Ovchinnikov, Q. Zheng, R. Hermann, S. Calder, B. Huang, Z. Fei, Y. Liu, X. Xu, M. A. McGuire, *ACS Nano* **2019**, *13*, 4436.
[33] S. Wu, Z. He, M. Gu, L. Ren, J. Li, B. Deng, D. Wang, X. Guo, W. Li, M. Chen, *Nat. Commun.* **2024**, *15*, 10765.
[34] C. Ahn, J. Lee, H. U. Kim, H. Bark, M. Jeon, G. H. Ryu, Z. Lee, G. Y. Yeom, K. Kim, J. Jung, *Adv. Mater.* **2015**, *27*, 5223.
[35] P. K. J. Wong, W. Zhang, F. Bussolotti, X. Yin, T. S. Herng, L. Zhang, Y. L. Huang, G. Vinai, S. Krishnamurthi, D. W. Bukhvalov, *Adv. Mater.* **2019**, *31*, 1901185.
[36] G. Kim, J. Lee, H. Seok, T. Kang, M. Lee, H. Choi, S. Son, J. Cho, D. Lee, S. Son, *Adv. Mater.* **2025**, *37*, 2419927.
[37] P. Sutter, S. Wimer, E. Sutter, *Nature* **2019**, *570*, 354.
[38] a) S. Falcinelli, F. Pirani, F. Vecchiocattivi, *Atmosphere* **2015**, *6*, 299; b) H. Seok, M. Kim, J. Cho, E. Kim, S. Son, K.-W. Kim, J. K. Kim, P. J. Yoo, M. Kim, H.-U. Kim, *ACS Sustainable Chem. Eng.* **2023**, *11*, 568.
[39] H. Seok, I. Lee, J. Cho, D. Sung, I.-K. Baek, C.-H. Lee, E. Kim, S. Jeon, K. Park, T. Kim, *Nanotechnology* **2021**, *33*, 025603.
[40] H. Seok, Y. T. Megra, C. K. Kanade, J. Cho, V. K. Kanade, M. Kim, I. Lee, P. J. Yoo, H.-U. Kim, J. W. Suk, *ACS Nano* **2021**, *15*, 707.
[41] C. Li, Y. An, *Phys. Rev. B* **2022**, *106*, 115417.
[42] J. Feng, D. Biswas, A. Rajan, M. D. Watson, F. Mazzola, O. J. Clark, K. Underwood, I. Markovic, M. McLaren, A. Hunter, *Nano Lett.* **2018**, *18*, 4493.